RSC Advances

PAPER

View Article Online
View Journal | View Issue

Cite this: *RSC Adv.*, 2024, **14**, 10507

Structure searches and superconductor discovery in XB_2 (X = Sc, Ti, V, Cr, and Tc)†

Jingjing Meng, [a] Pengyu Zheng,[a] Yiran Peng,[a] Rui Liu,[a] Ying Yang[a] and Zhiping Yin *[ab]

Received 22nd December 2023
Accepted 11th March 2024

DOI: 10.1039/d3ra08746h

rsc.li/rsc-advances

With extensive structure searches for XB_2 (X = Sc, Ti, V, Cr, and Tc) under pressures up to 100 GPa, we uncovered that the crystal structures of these compounds with the lowest enthalpy have the same space group (*P6/mmm*) as MgB_2 at ambient pressure. Among them, ScB_2, TiB_2 and VB_2 are dynamically stable at ambient pressure, but they do not superconduct. CrB_2 becomes dynamically stable at 108 GPa and shows superconductivity with a transition temperature (T_c) of 26.0 K. TcB_2 is not dynamically stable until 9 GPa. At 20 GPa, it has a T_c of 23.5 K. Further calculations indicate that CrB_2 and TcB_2 are also thermodynamically stable, suggesting that it is highly likely that they can be synthesized successfully in the laboratory. We found that transition metal atoms (Cr/Tc) dominate soft phonon vibrations and make significant contributions to the electron–phonon coupling (EPC) and superconductivity in CrB_2/TcB_2, which is in strong contrast to the case of MgB_2, where high-frequency B vibrations dominate the EPC and superconductivity. Our work enriches the understanding of superconductivity in transition metal borides.

1 Introduction

Searching for high transition temperature (high-T_c) superconductors has been an active research area in condensed matter physics and material sciences for a long time. Since the discovery of superconductivity in 2001, MgB_2 has attracted the attention of researchers worldwide. Extensive work has been done on this compound,[1–14] including some impressive theoretical investigations that have provided important insights.[1–5,14] MgB_2 is a conventional BCS superconductor with a T_c of 39 K.[15] First-principles calculations have revealed its electronic structure, phonon spectra, and EPC.[3,12,13] As a metallic layered compound[10] with multiple bands crossing the Fermi level, MgB_2 comprises fully ionized Mg atoms[5] and exhibits strong covalent bonds among B atoms within its honeycomb layer. Moreover, this compound manifests metallic bonds between different B layers, contributing to its distinctive characteristics.[3] Further research indicates that the E_{2g} mode involving the in-plane vibration of two boron ions in opposite directions contributes significantly to its superconductivity.[2] Given the remarkable performance of MgB_2, researchers have turned to investigating other boride compounds,[16–35] such as LiBC and Ca–B, Be–B, and Y–B binary compounds. Many materials, for example, B_{24}, MgB_6, GaB_5, InB_6, and CaB_6, have been confirmed to be superconductors.[16,19,20,29,36] However, the T_c of these superconductors is generally much lower than that of MgB_2.

Transition metal borides have usually appeared as superhard materials in previous studies. For example, TiB_2, the compound with the lowest density and highest hardness among the metal borides, is an important modern ceramic material.[37] In recent years, with an improvement in experimental equipment, researchers have been able to obtain new materials under very high pressures in the laboratory. For example, in 2015, SH_3 was synthesized and compressed up to 250 GPa experimentally by A. Drozdov *et al.* using a diamond anvil cell (DAC),[38] which has a T_c value between 191 K and 204 K at 200 GPa.[38,39] With this technique, a transition-metal boride MoB_2 was experimentally discovered at about 100 GPa, which sparked great excitement among researchers because it has a high T_c of 32 K.[36] This breakthrough indicates it would be interesting to investigate other transition metal borides.

In this work, we search the crystal structures of five transition metal borides (ScB_2, TiB_2, VB_2, CrB_2, and TcB_2) under pressures up to 100 GPa using an efficient structural prediction method called Crystal Structure Analysis by Particle Swarm Optimization (*i.e.*, the CALYPSO code).[40–42] We find that the crystal structures of XB_2 (X = Sc, Ti, V, Cr, and Tc) with the lowest enthalpy have the same space group (*P6/mmm*) as MgB_2 at ambient pressure. Among them, ScB_2, TiB_2 and VB_2 are dynamically stable without superconductivity at ambient pressure. CrB_2 and TcB_2 become dynamically stable under 108 GPa and 9 GPa, respectively. CrB_2 and TcB_2 are conventional superconductors with high EPC strength and superconducting temperatures up to 26.0 K (at 108 GPa) and 23.5 K (at 20 GPa), respectively. The strong electron–phonon coupling comes

[a]*Department of Physics, Center for Advanced Quantum Studies, Beijing Normal University, Beijing 100875, China. E-mail: yinzhiping@bnu.edu.cn*

[b]*Key Laboratory of Multiscale Spin Physics, Ministry of Education, Beijing Normal University, Beijing 100875, China*

† Electronic supplementary information (ESI) available. See DOI: https://doi.org/10.1039/d3ra08746h

mostly from low-frequency acoustic phonon modes involving mainly vibrations of the transition metal atoms, whose d electrons dominate electronic states around the Fermi level. This is in strong contrast to MgB_2 whose moderate electron–phonon coupling is mainly contributed by B atoms. Interestingly, the electron–phonon coupling and superconducting temperature in TcB_2 show very weak pressure dependence in the studied pressure range of 20–100 GPa.

2 Computational methods

We explore the crystal structures of XB_2 (X = Sc, Ti, V, Cr, and Tc) from ambient pressure to 100 GPa using fixed composition calculations with cells containing 1–4 formula units implemented in the CALYPSO code.[40–42] In this study, the number of generations is set to 50, and the population size is set to 30. Crystal structures are generated randomly in the first generation. In each subsequent generation, 60% of the structures are generated from the lowest-enthalpy structures provided by the previous generation; the remaining 40% are generated randomly.

The CALYPSO software employs a set of special structural evolution techniques.[40–42] However, it relies on third-party software to optimize and compute the enthalpies of the crystal structures generated by CALYPSO. In this study, we employ the VASP code[43,44] to relax the structures with the generalized gradient approximation (GGA)[45] employing the projected augmentation wave method.[46] We employ a plane-wave cut-off energy of 420 eV and k-mesh with a grid spacing of 0.20 $Å^{-1}$. The relaxation continues until the forces on all atoms become smaller than 10^{-3} eV $Å^{-1}$ while maintaining an electronic self-consistency threshold of 10^{-6} eV per cell.

Finally, we select the crystal structure with the lowest enthalpy of each composition under various pressures produced by CALYPSO and calculate their electronic properties using VASP. To further investigate the lattice dynamics and electron–phonon coupling of these materials, we employ density functional perturbation theory (DFPT)[47] implemented in the QUANTUM ESPRESSO[48] package to compute these properties. The Perdew–Burke–Ernzerhof (PBE)[49] exchange-correlation function is utilized, along with 18 × 18 × 18 Monkhorst–Pack k-point grids. Norm-conserving PBE pseudopotentials[50] with a cutoff energy of 90 Ry are used for wave functions. Dynamical matrices are calculated on a 6 × 6 × 6 q-point mesh. Finally, we estimate the superconducting critical temperature (T_c) using the Allen–Dynes–McMillan equation[51] with a typical value of the Coulomb pseudopotential $\mu^* = 0.1$.

3 Theoretical background

According to the Bardeen–Cooper–Schrieffer (BCS) theory of superconductivity, there is a relationship among the superconducting transition temperature T_c, the typical phonon energy $\langle\omega\rangle$ and interaction strength $N(0)V$:[52]

$$T_c = 1.14\langle\omega\rangle\exp[-1/N(0)V]. \quad (1)$$

here, $N(0)$ is the electronic density of states at the Fermi level; V is the pairing potential arising from the electron–phonon interaction.

Since the BCS theory was proposed,[53] significant advances have been made in comprehending the role of the electron–phonon interaction in normal and superconducting metals.[52] Among them, the Eliashberg equations represent the state of the art in the theory of conventional superconductivity.[52] Subsequently, the most extensive study of the relation between microscopic theory and observed superconducting transition temperature was made by McMillan. The McMillan equation is a significant accumulation of microscopic information on strong-coupling superconductors by solving the finite-temperature Eliashberg theory to find T_c.[51] The total EPC constant λ is obtained *via* the isotropic Eliashberg function:[51,52,54]

$$\alpha^2F(\omega) = \frac{1}{2\pi N(E_F)}\sum_{\mathbf{q}\nu}\delta(\omega-\omega_{\mathbf{q}\nu})\frac{\gamma_{\mathbf{q}\nu}}{\omega_{\mathbf{q}\nu}}, \quad (2)$$

$$\lambda = 2\int\frac{\alpha^2F(\omega)}{\omega}\mathrm{d}\omega = \sum_{\mathbf{q}\nu}\lambda_{\mathbf{q}\nu}, \quad (3)$$

The parameter λ, which roughly corresponds to $N(0)V$ in the BCS theory, serves as a dimensionless measure of the strength of α^2F.

$\alpha^2F(\omega)$ is the Eliashberg function, $F(\omega)$ is the phonon density of states, α^2 is an average of the electron–phonon interaction, $N(E_F)$ is the DOS at the Fermi level, $\omega_{\mathbf{q}\nu}$ is the phonon frequency of the νth phonon mode with wave vector $\mathbf{q}$, and $\gamma_{\mathbf{q}\nu}$ is the phonon linewidth, which can be estimated by[51]

$$\gamma_{\mathbf{q}\nu} = \frac{2\pi\omega_{\mathbf{q}\nu}}{\Omega_{BZ}}\sum_{\boldsymbol{k},m,n}\left|g^{\nu}_{\boldsymbol{k}n,\boldsymbol{k}+\mathbf{q}m}\right|^2\delta(\varepsilon_{\boldsymbol{k}n}-E_F)\times\delta(\varepsilon_{\boldsymbol{k}+\mathbf{q}m}-E_F), \quad (4)$$

where Ω_{BZ} is the volume of the first Brillouin zone, $\varepsilon_{\boldsymbol{k}n}$ and $\varepsilon_{\boldsymbol{k}+\mathbf{q}m}$ indicate the Kohn–Sham energy and $g^{\nu}_{\boldsymbol{k}n,\boldsymbol{k}+\mathbf{q}m}$ represents the screened electron–phonon matrix element. $\lambda_{\mathbf{q}\nu}$ is the EPC constant for phonon mode $\mathbf{q}\nu$,[51,52,54] which is defined as:

$$\lambda_{\mathbf{q}\nu} = \frac{\gamma_{\mathbf{q}\nu}}{\pi\hbar N(E_F)\omega_{\mathbf{q}\nu}{}^2}, \quad (5)$$

T_c is estimated using the McMillan–Allen–Dynes formula:[51]

$$T_c = \frac{\omega_{\log}}{1.2}\exp\left(\frac{-1.04(1+\lambda)}{\lambda-\mu^*(1+0.6\lambda)}\right), \quad (6)$$

The hysteretic Coulomb pseudopotential μ^* in eqn (6) is set to a typical value of 0.1, and the logarithmic average of the phonon frequencies $\omega_{\log}$ is defined as[51]

$$\omega_{\log} = \exp\left[\frac{2}{\lambda}\int\alpha^2F(\omega)\frac{\ln\omega}{\omega}\mathrm{d}\omega\right]. \quad (7)$$

4 Results and discussions

In our structural searches, ScB_2, TiB_2 and VB_2 are dynamically stable at ambient pressure with no imaginary frequency in their

phonon–dispersion curves (shown in Fig. S1†). Table SI† shows that their formation enthalpies are −0.85, −1.08, and −0.73 eV per atom, respectively. The EPC strength is 0.28 for ScB_2, 0.1 for TiB_2 and 0.3 for VB_2, which are too weak to support conventional superconductivity in these materials. Information on their crystal structures is shown in Table SI.†

The phonon–dispersion curve of CrB_2 has imaginary frequencies under pressures until 108 GPa. For TcB_2, it turns to be dynamically stable at 9 GPa. However, the phonon–dispersion curves of TcB_2 exhibit a significant softening at 9 GPa and 10 GPa (shown in Fig. S2†), suggesting that the structures may be unstable in the laboratory. Therefore, we discuss the physical properties of TcB_2 at 20 GPa as being typical. In the following, we will focus on investigating the crystal structures, electronic properties, lattice dynamics and superconductivity of CrB_2 at 108 GPa and TcB_2 at 20 GPa.

4.1 Physical properties of CrB_2

4.1.1 Crystal structure and electronic properties. The primitive cell of CrB_2 contains one Cr atom and two equivalent B atoms with lattice constants $a = 2.80$ Å and $c = 2.62$ Å at 108 GPa. As shown in Table 1, the intralayer B–B bond length is 1.61 Å, and the bond length for the nearest Cr–B is 2.08 Å. The electron localization function (ELF) value for B–B bonds is calculated to be 0.82 (as shown in Fig. S3†), indicating their covalent bonding nature. The ELF value between the nearest Cr–B atoms is approximately 0.55, suggesting a metallic character. As pressure increases, a reduction in lattice parameters is observed. Specifically, at 150 GPa, the lattice parameter a decreases to 2.75 Å and c decreases to 2.56 Å. The intralayer B–B bond length is also reduced to 1.59 Å, while the bond length for the nearest Cr–B is reduced to approximately 2.04 Å. The formation enthalpy of compound A_xB_y is defined as $\Delta H = (H_{A_xB_y} - xH_A - yH_B)/(x + y)$, where $H_{A_xB_y}$, H_A, and H_B are the enthalpies of compound A_xB_y, element A and element B, respectively. The values are −1.30 eV per atom and −1.36 eV per atom for CrB_2 at 108 GPa and 150 GPa, respectively, indicating that it is an exothermic reaction. Therefore, it is highly likely that CrB_2 can be synthesized experimentally from a thermodynamic point of view.

To analyse electronic properties, we plot the band structure and electronic density of states (DOS) in Fig. 1. Herein, we project Cr-d orbitals and B-p orbitals (relevant to our discussion) onto the band structure. The orbital-resolved band structure shows metallic characteristics with three bands crossing the Fermi level. The DOS reveals that overlaps between the two elements are moderate, and the total DOS at the Fermi level is 1.49 states per eV. As can be seen in Fig. 1, Cr-d orbitals play a dominant role around the Fermi level. Since the EPC

Table 1 Lattice parameters, formation enthalpy, bond length for the nearest Cr–B and intralayer B–B bonding, the calculated EPC strength (λ), logarithmic average phonon frequency (ω_{log}), and the estimated T_c for CrB_2 at 108 GPa and 150 GPa

Compound	Lattice parameters (Å)		λ	ω_{log} (meV)	T_c (K)	Pressure (GPa)	Formation enthalpy (eV per atom)	Bond lengths (Å)	
	a	c						B–B	Cr–B
CrB_2	2.8	2.62	1.4	21.2	26.0	108	−1.30	1.61	2.08
CrB_2	2.75	2.56	0.75	38.9	18.3	150	−1.36	1.59	2.04

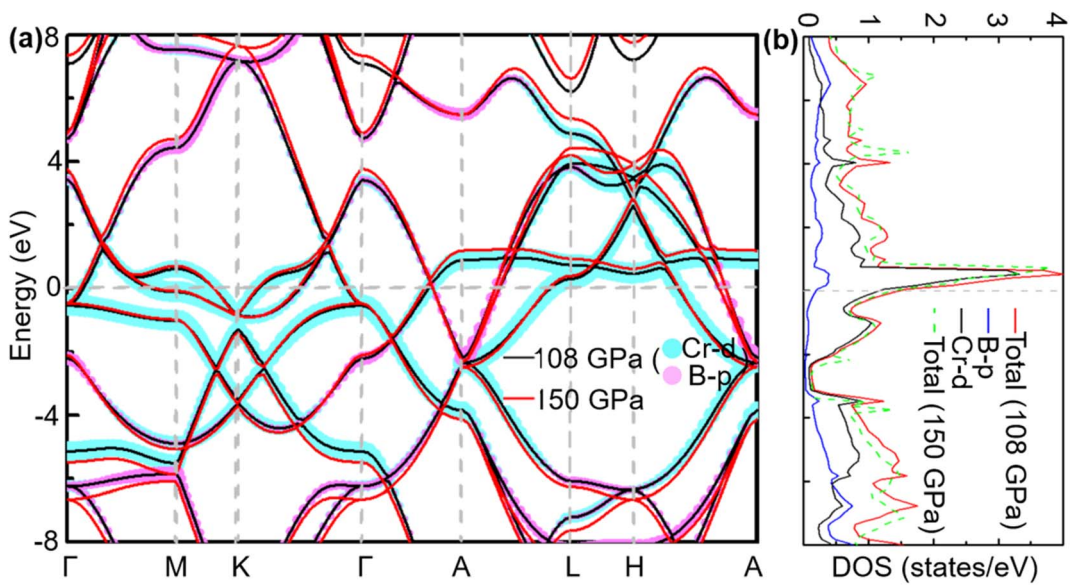

Fig. 1 (a) Calculated band structure, (b) total DOS, and projected DOS near the Fermi level of CrB_2 at 108 GPa (band structure and total DOS at 150 GPa are also plotted for comparison). The cyan and pink broad bands reflect the amounts of Cr-d and B-p orbital character.

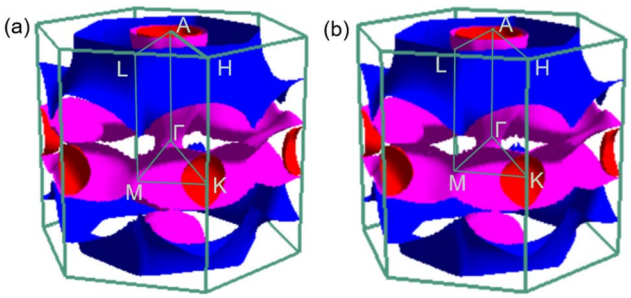

Fig. 2 Fermi surfaces of CrB_2 in the first Brillouin zone at (a) 108 GPa and (b) 150 GPa.

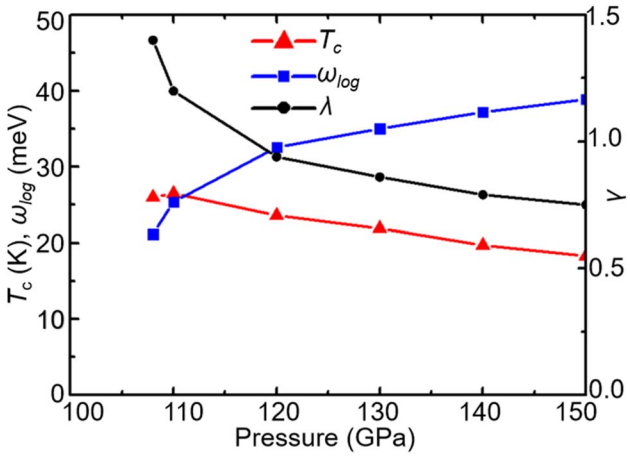

Fig. 4 Pressure dependence of T_c, ω_{log}, and λ in CrB_2.

parameter λ corresponds roughly to $N(E_F)V$ in the BCS theory, we can speculate that Cr-d orbitals near the Fermi level are closely related to EPC and superconductivity in CrB_2. Comparison of band structures at 108 GPa and 150 GPa reveals that most bands around the Fermi level remain unchanged except those near the *A* point, resulting in nearly identical Fermi surfaces. Therefore, the pressure has little effect on its Fermi surfaces. However, a decrease of approximately 8.1% in the total DOS at the Fermi level is observed at 150 GPa from that at 108 GPa (Fig. 2).

4.1.2 Lattice dynamics and electron–phonon coupling. To explore the lattice dynamics and potential conventional superconductivity of CrB_2, we calculate and show in Fig. 3 the phonon dispersion, phonon density of states (PhDOS), Eliashberg spectral function, $\alpha^2F(\omega)$, and EPC integral, $\lambda(\omega)$. As can be seen from phonon dispersion curves, there are no imaginary frequencies in the whole phonon–dispersion curves of CrB_2, indicating that CrB_2 at 108 GPa is dynamically stable. The PhDOS reveals that the low-frequency region (below 45 meV) of the phonon–dispersion curves is primarily contributed by the vibration of the Cr atom, while higher frequencies above 62 meV are mainly attributed to the vibrations of the two equivalent B atoms. Due to the significant difference in atomic mass between Cr and B, there is a gap between low-frequency acoustic and high-frequency optical phonon branches. As can be seen from the Eliashberg spectral function $\alpha^2F(\omega)$ and EPC $\lambda(\omega)$, low-frequency vibrations of Cr atoms contribute more than 90% of the total EPC. This is mainly because the electronic states around the Fermi level are dominated by Cr-d electrons. From the mode- and momentum-resolved EPC $\lambda_{\mathbf{q}\nu}$ shown in Fig. 3(a), it is evident that the total EPC comes mainly from the acoustic phonon modes near the $\boldsymbol{q}$ point (0.167, 0.167, and 0.5), which involves primarily Cr atoms moving along the *c* direction.

With increasing pressure, as shown in Fig. 4, T_c rises slightly at 110 GPa and later shows a decreasing tendency. According to the phonon dispersion curves with the strength of mode- and $\boldsymbol{q}$-resolved $\lambda_{\mathbf{q}\nu}$ illustrated in Fig. 5, all phonon modes shift towards higher frequencies with increasing pressure, as expected. Meanwhile, there is an apparent decrease in the aforementioned strong electron–phonon coupling of the acoustic phonon mode around the $\boldsymbol{q}$ point (0.167, 0.167, and 0.5) with increasing pressure, accompanied by hardening of the corresponding phonon mode. Taking 108 GPa and 150 GPa for example, the logarithmic average phonon frequency (ω_{log}) increases from

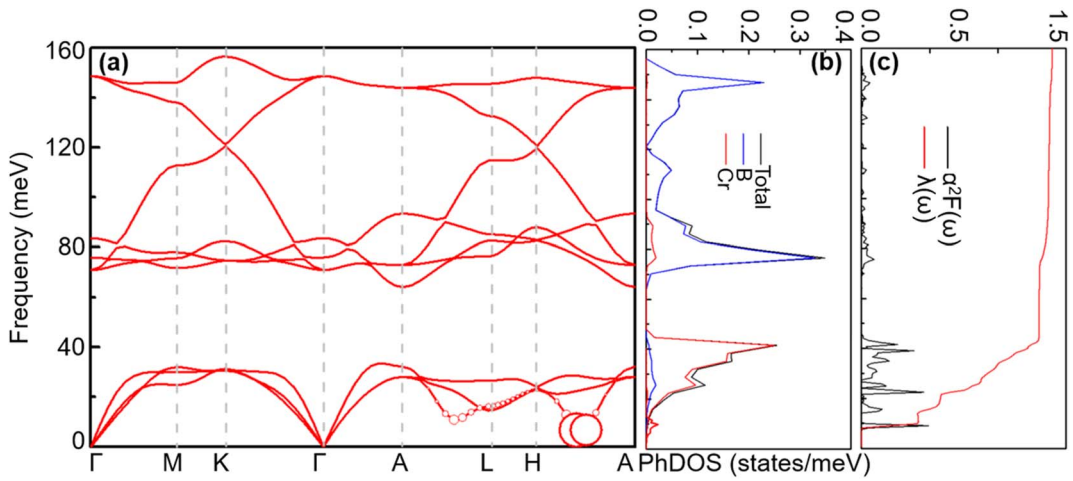

Fig. 3 (a) Phonon spectra, (b) total and projected phonon DOS, (c) Eliashberg spectral function $\alpha^2F(\omega)$ and $\lambda(\omega) = 2\int \alpha^2F(\omega)/\omega d\omega$ (right) for CrB_2 at 108 GPa. Red solid circles represent the mode-dependent EPC with the radius proportional to the respective coupling strength.

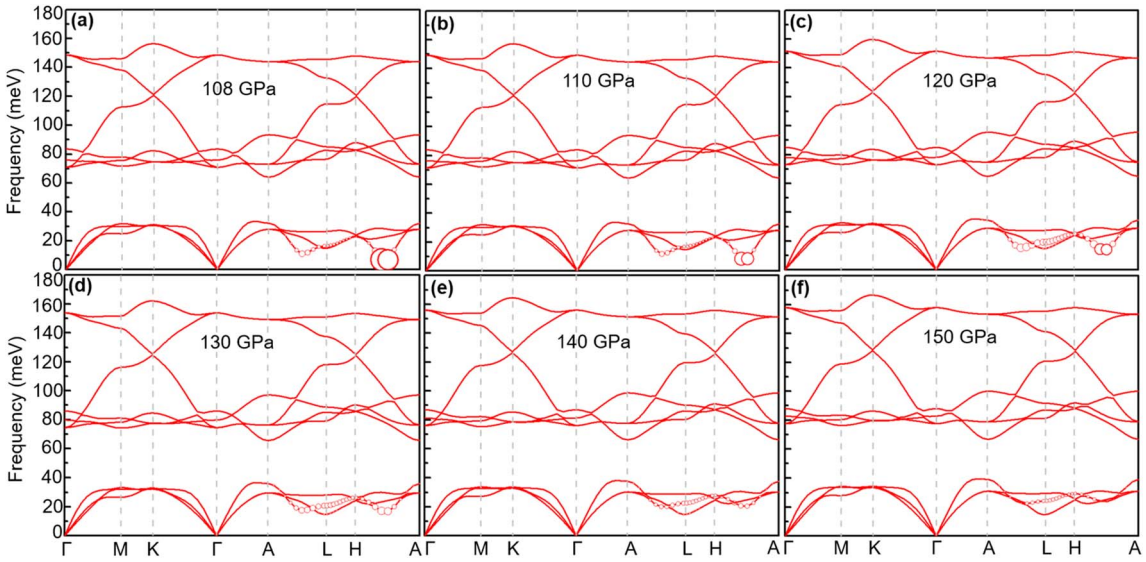

Fig. 5 Phonon spectra of CrB_2 at different pressures: (a) 108 GPa, (b) 110 GPa, (c) 120 GPa, (d) 130 GPa, (e) 140 GPa, and (f) 150 GPa. The radius of the red solid circle is proportional to the mode-dependent EPC strength (the scaling factors of coupling strength for 120, 130, 140, and 150 GPa are enlarged by a factor of 2.5).

21.2 meV to 38.9 meV, whereas the EPC parameter (λ) decreases from 1.40 to 0.75, as shown in Table 1. As a result, T_c decreases from 26 K to 18.3 K.

4.2 Physical properties of TcB_2

4.2.1 Crystal structure and electronic properties. The crystal structure of TcB_2 we obtained at 20 GPa differs slightly from the structure used by E. Deligoz and coworkers at ambient pressure.[55] As shown in Table 2 and Fig. S3,† the lattice parameters of TcB_2 are $a = 2.9$ Å and $c = 3.31$ Å at 20 GPa. The intralayer B–B bond is 1.68 Å with an ELF value of 0.83, which is typical for covalent bonding. The nearest Tc–B distance is 2.36 Å with an ELF value of about 0.5, which shows a metallic character. With increasing pressure, lattice parameters become smaller. At 100 GPa, the lattice parameters decrease to $a = 2.76$ Å and $c = 3.15$ Å. The intralayer B–B bond length becomes 1.59 Å, and the nearest Tc–B distance is 2.24 Å. The formation enthalpies of TcB_2 are −0.31 eV per atom and −0.87 eV per atom at 20 GPa and 100 GPa, respectively, which are also exothermic reactions. Therefore, TcB_2 can be synthesized experimentally from a thermodynamic point of view at 20 GPa and 100 GPa.

As shown in Fig. 6, the electronic structure of TcB_2 is similar to that of CrB_2. The DOS near the Fermi level is mostly contributed by Tc-d orbitals, whereas the B-p orbitals contribute only a rather small portion. The band structure with four bands crossing the Fermi level shows metallic characteristics. The total DOS at the Fermi level is 1.34 states per eV at 20 GPa. Compared with CrB_2, the DOS of TcB_2 is not so localized and is more evenly distributed around the Fermi level. With increasing pressure from 20 GPa to 100 GPa, the total DOS at the Fermi level decreases by 10.5%. The band shifting around the Fermi level is more pronounced than that in CrB_2. The most significant distinction among the Fermi surfaces can be observed in the blue region shown in Fig. 7, where an enlargement occurs around these sheets under increasing pressure. Furthermore, there is an increase in size for the spherical Fermi surface centered at point *A*.

4.2.2 Lattice dynamics and electron–phonon coupling. Previous studies[56] have shown that TcB_2 is a fairly hard material. In 2012, Deligoz and collaborators investigated the vibrational properties of TcB_2,[55] whereas the electron–phonon coupling and superconducting properties are still unknown. In this part, we study the phonon dispersion, PhDOS, Eliashberg spectral function, $\alpha^2F(\omega)$, and EPC integral $\lambda(\omega)$ of TcB_2 to explore its electron–phonon coupling and superconducting properties. As shown in Fig. 8, the overall features of the phonon dispersion curves are similar to those of TcB_2 in Deligoz's paper.[55] TcB_2 at 20 GPa is dynamically stable with no imaginary frequencies in

Table 2 Lattice parameters, formation enthalpy, bond length for the nearest Tc–B and intralayer B–B bonding, the calculated EPC strength (λ), logarithmic average phonon frequency (ω_{log}), and the estimated T_c for TcB_2 at different pressures

Compound	Lattice parameters (Å)		λ	ω_{log} (meV)	T_c (K)	Pressure (GPa)	Formation enthalpy (eV per atom)	Bond lengths (Å)	
	a	c						B–B	Tc–B
TcB_2	2.9	3.31	1.61	16.7	23.5	20	−0.31	1.68	2.36
TcB_2	2.76	3.15	0.97	26.8	20.6	100	−0.87	1.59	2.24

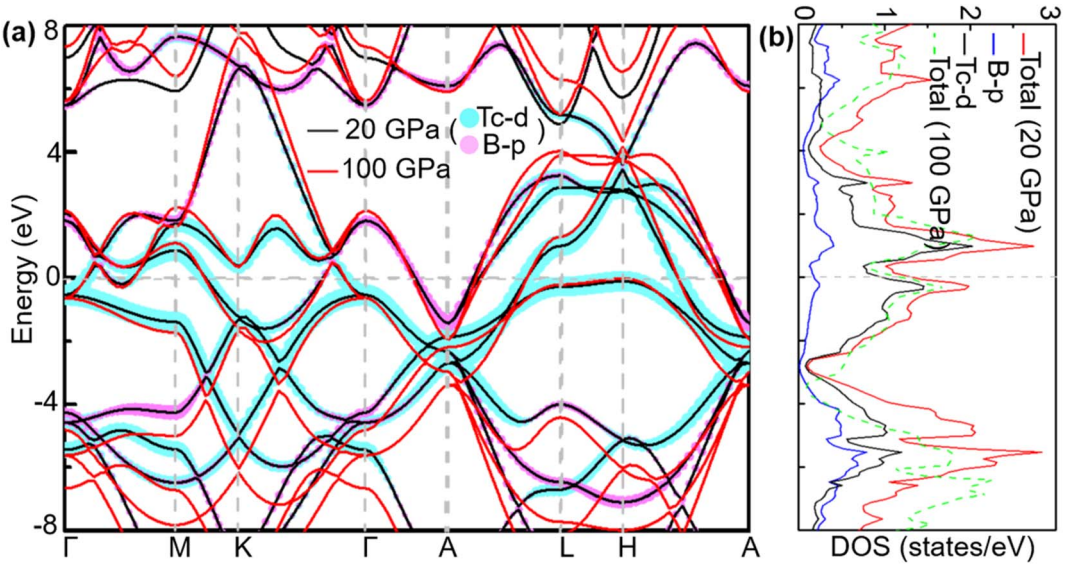

Fig. 6 (a) Calculated band structure, (b) total DOS, and projected DOS near the Fermi level of TcB_2 at 20 GPa (band structure and total DOS at 100 GPa are also plotted for comparison). The cyan and pink broad bands reflect the amounts of Tc-d and B-p orbital character.

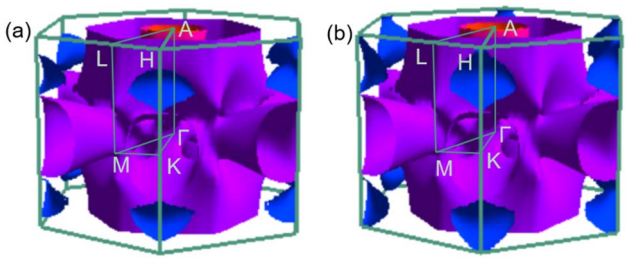

Fig. 7 Fermi surfaces of TcB_2 in the first Brillouin zone (a) at 20 GPa and (b) at 100 GPa.

its phonon spectra. The high-frequency optical modes come mostly from the vibrations of B atoms, while the vibrations of Tc atoms mainly contribute to the low-frequency acoustic modes. Around 20 meV, a distinct gap exists between the low-frequency acoustic and high-frequency optical phonon modes. We note that there are some subtle differences between the phonon spectra in Fig. 8 and that reported in ref. 55. The most notable difference is that our phonon spectra soften more severely in acoustic branches, which is usually caused by strong electron–phonon interaction. Indeed, as shown in Fig. 8(c), the integrated electron–phonon coupling $\lambda(\omega)$ grows rapidly in the low-frequency region (0–24.6 meV), which makes a dominant contribution (about 88%) to the total EPC λ of 1.61. The high-

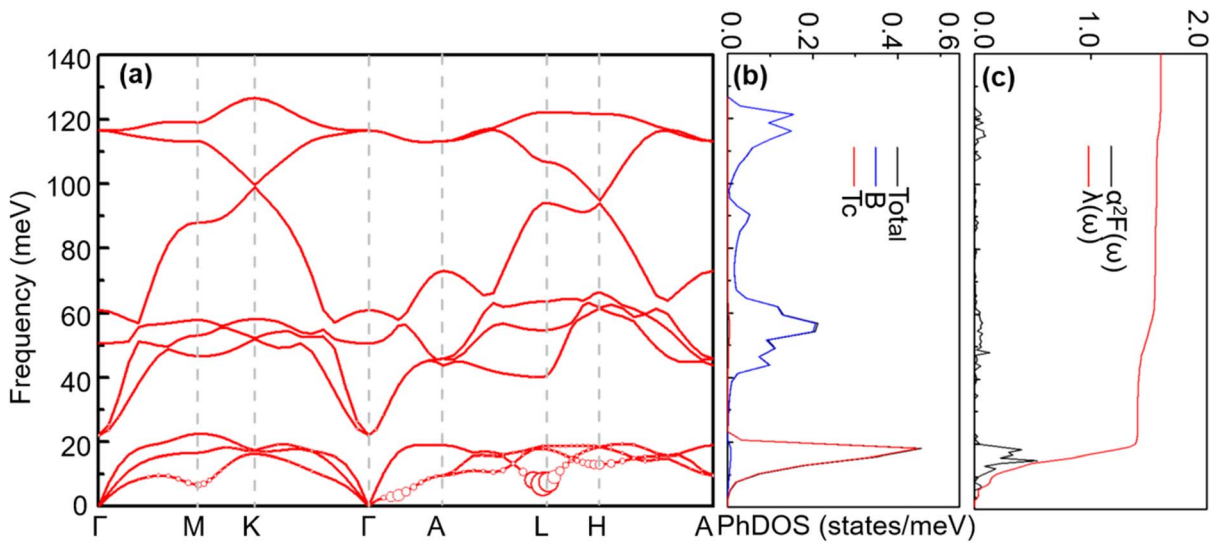

Fig. 8 (a) Phonon spectra, (b) total and projected phonon DOS, (c) Eliashberg spectral function $\alpha^2F(\omega)$ and $\lambda(\omega) = 2\int \alpha^2F(\omega)/\omega d\omega$ (right) for TcB_2 at 20 GPa. Red solid circles represent the mode-dependent EPC with the radius proportional to the respective coupling strength.

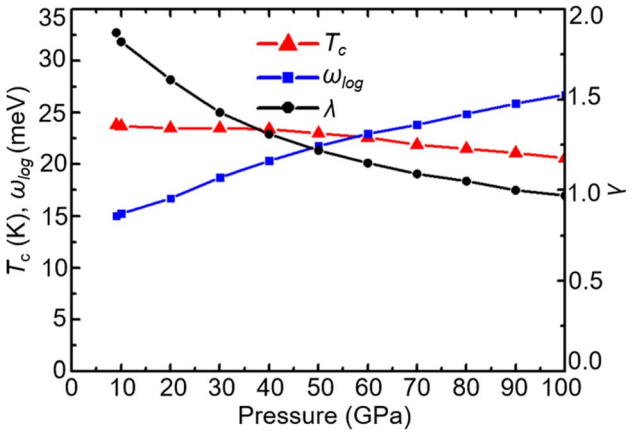

Fig. 9 Pressure dependence of T_c, ω_{log}, and λ in TcB_2.

frequency part (24.6–127 meV) dominated by vibrations of B atoms contributes only about 12%. We find an acoustic mode around point L that contributes significantly to the EPC, which mainly involves vibrations of the Tc atoms moving along the [1 2 0] direction.

When the pressure increases from 20 GPa to 100 GPa, while the logarithmic average phonon frequency ω_{log} increases, the total EPC λ and superconducting temperature T_c decrease with pressure, as shown in Fig. 9. Fig. 10 shows the phonon spectra with mode- and momentum-dependent EPC $\lambda_{q\nu}$ of TcB_2 at different pressures from 20 GPa to 100 GPa. It is evident that all the phonon modes are shifted to higher frequencies with increasing pressure. As shown in Table 2, the logarithmic average phonon frequency increases from 16.7 meV at 20 GPa to 26.8 meV at 100 GPa, whereas the total EPC λ decreases from 1.61 to 0.97, and the superconducting temperature T_c decreases from 23.5 K to 20.6 K correspondingly. In contrast to CrB_2, the aforementioned most important phonon mode, *i.e.*, the acoustic phonon mode around point L dominated by in-plane vibrations of the Tc atoms, shows little change in the mode-dependent EPC $\lambda_{q\nu}$ and almost no hardening of the phonons with increasing pressure. Instead, the EPC $\lambda_{q\nu}$ of the lowest acoustic phonon along Γ–A and around point H decrease substantially with increasing pressure, which is responsible for the corresponding reduction of the total EPC and EPC λ and superconducting temperature T_c as the pressure increases. As a result, the decreasing rate of the total EPC λ with increasing pressure in TcB_2 is only half the value in CrB_2 (0.008/GPa *vs.* 0.015/GPa). More importantly, this leads to a much slower rate of decrease of the superconducting temperature T_c of 0.036 K GPa^{-1} in TcB_2 compared to 0.18 K GPa^{-1} in CrB_2 over the pressure range studied.

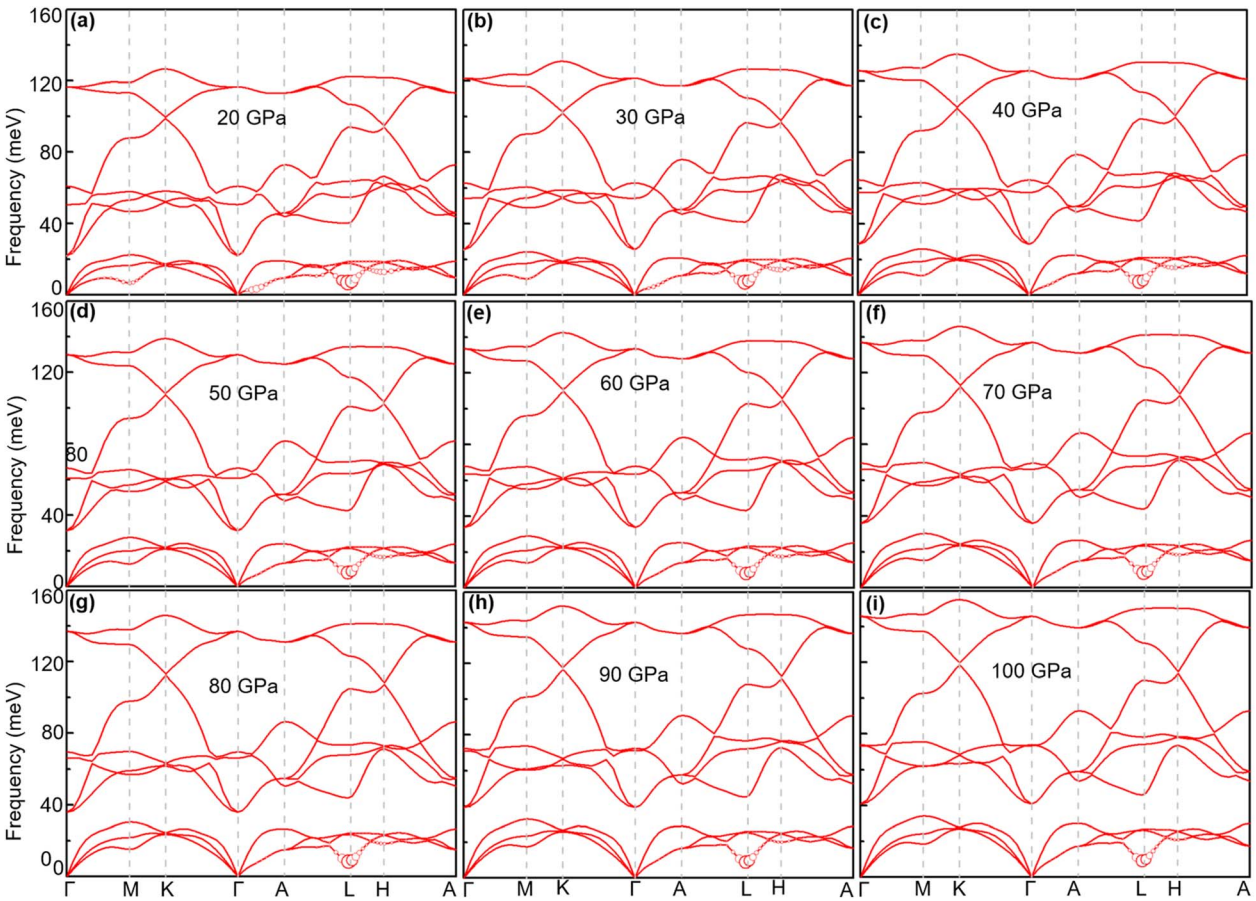

Fig. 10 Phonon spectra of TcB_2 at different pressures: (a) 20 GPa, (b) 30 GPa, (c) 40 GPa, (d) 50 GPa, (e) 60 GPa, (f) 70 GPa, (g) 80 GPa, (h) 90 GPa, and (i) 100 GPa. The radius of the red solid circle is proportional to the mode-dependent EPC strength.

5 Conclusion

We carried out an extensive structure search and found that all five XB_2 (X = Sc, Ti, V, Cr, and Tc) crystallize in the *P*6/*mmm* space group under pressures up to 100 GPa. Unlike MoB_2, which has a structural phase transition at 70 GPa, none of the XB_2 (X = Sc, Ti, V, Cr, and Tc) undergoes a phase transition below 100 GPa. Among them, ScB_2, TiB_2, and VB_2 are dynamically stable at ambient pressure but are not conventional superconductors. On the other hand, CrB_2 becomes dynamically stable when it transforms into a conventional superconductor at 108 GPa with a critical superconducting temperature T_c of 26.0 K. With increasing pressure, its T_c rises slightly at 110 GPa and gradually decreases to 18.3 K at 150 GPa. TcB_2 is also a conventional superconductor within the pressure range 20–100 GPa, with less dependence of T_c on pressure. Its T_c is 23.5 K at 20 GPa and 20.6 K at 100 GPa. In addition, the negative formation enthalpy and absence of imaginary phonon frequency suggest that it is possible to synthesize both CrB_2 and TcB_2 successfully in experiments.

In both CrB_2 and TcB_2, the electronic states around the Fermi level mainly come from the d electrons of the transition metal atoms Cr/Tc, suggesting the electron–phonon coupling is dominated by the transition metal atoms instead of boron atoms, in strong contrast to MgB_2 where the EPC comes mainly from the B atoms. Most of the strong total EPC ($\lambda > 1$) in both CrB_2 and TcB_2 comes from the low-frequency acoustic phonon modes involving vibrations of the transition metal atoms, which is similar to the case of MoB_2.[36] In CrB_2, the acoustic phonon mode around $\boldsymbol{q} = (0.167, 0.167, \text{and } 0.5)$ with Cr atoms moving along the *c*-axis has dominated the EPC mode, which decreases rapidly with increasing pressure. On the contrary, in TcB_2, the acoustic phonon mode around the *L* point (0.5, 0, and 0.5) with Cr atoms moving in the *ab*-plane has dominated the EPC mode, which shows very weak pressure dependence. As a result, the superconducting temperature in TcB_2 has very weak pressure dependence. Combined with the relatively low pressure of 20 GPa and high T_c of 23.5 K, TcB_2 is perhaps the most interesting transition metal boride studied so far.

Author contributions

Z. P. Yin conceived and directed this project. J. J. Meng performed structure searches and DFT and DFPT calculations. All the authors participated in discussing the results and writing the manuscript.

Conflicts of interest

There are no conflicts of interest to declare.

Acknowledgements

This work was supported by the National Natural Science Foundation of China (Grant No. 12074041 and 11674030) and the National Key Research and Development Program of China through Contract No. 2016YFA0302300. The calculations were carried out using the high-performance computing cluster of Beijing Normal University in Zhuhai.

Notes and references

1 H. J. Choi, D. Roundy, H. Sun, M. L. Cohen and S. G. Louie, *Nature*, 2002, **418**, 758–760.
2 J. A. Alarco, A. Chou, P. C. Talbot and I. D. Mackinnon, *Phys. Chem. Chem. Phys.*, 2014, **16**, 24443–24456.
3 I. Mazin and V. Antropov, *Phys. C*, 2003, **385**, 49–65.
4 J. Alarco, P. Talbot and I. Mackinnon, *Model. Numer. Simul. Mater. Sci.*, 2018, **8**, 8374921–8374946.
5 J. Kortus, I. I. Mazin, K. D. Belashchenko, V. P. Antropov and L. L. Boyer, *Phys. Rev. Lett.*, 2001, **86**, 4656–4659.
6 J. M. Rowell, *Supercond. Sci. Technol.*, 2003, **16**, R17.
7 M. Eisterer, *Supercond. Sci. Technol.*, 2007, **20**, R47.
8 W. Kang, H.-J. Kim, E.-M. Choi, C. U. Jung and S.-I. Lee, *Science*, 2001, **292**, 1521–1523.
9 F. Bouquet, Y. Wang, R. Fisher, D. Hinks, J. Jorgensen, A. Junod and N. Phillips, *Europhys. Lett.*, 2001, **56**, 856.
10 X. Xi, *Rep. Prog. Phys.*, 2008, **71**, 116501.
11 C. Buzea and T. Yamashita, *Supercond. Sci. Technol.*, 2001, **14**, R115.
12 H. J. Choi, M. L. Cohen and S. G. Louie, *Phys. C*, 2003, **385**, 66–74.
13 J. Kortus, *Phys. C*, 2007, **456**, 54–62.
14 J. An and W. Pickett, *Phys. Rev. Lett.*, 2001, **86**, 4366.
15 J. Nagamatsu, N. Nakagawa, T. Muranaka, Y. Zenitani and J. Akimitsu, *Nature*, 2001, **410**, 63–64.
16 S. Shah and A. N. Kolmogorov, *Phys. Rev. B: Condens. Matter Mater. Phys.*, 2013, **88**, 014107.
17 S. Okatov, A. Ivanovskii, Y. E. Medvedeva and N. Medvedeva, *Phys. Status Solidi B*, 2001, **225**, R3–R5.
18 D. V. Rybkovskiy, A. G. Kvashnin, Y. A. Kvashnina and A. R. Oganov, *J. Phys. Chem. Lett.*, 2020, **11**, 2393–2401.
19 L. Yan, T. Bo, P.-F. Liu, L. Zhou, J. Zhang, M.-H. Tang, Y.-G. Xiao and B.-T. Wang, *J. Mater. Chem. C*, 2020, **8**, 1704–1714.
20 T. Bo, P.-F. Liu, L. Yan and B.-T. Wang, *Phys. Rev. Mater.*, 2020, **4**, 114802.
21 H. Rosner, A. Kitaigorodsky and W. Pickett, *Phys. Rev. Lett.*, 2002, **88**, 127001.
22 E. Deligoz, K. Colakoglu and Y. Ciftci, *Solid State Commun.*, 2009, **149**, 1843–1848.
23 K. Togano, P. Badica, Y. Nakamori, S. Orimo, H. Takeya and K. Hirata, *Phys. Rev. Lett.*, 2004, **93**, 247004.
24 Y. Liang, M. Xu, Z. Qu, S. Lin, J. Hao and Y. Li, *J. Mater. Chem. C*, 2021, **9**, 8258–8264.
25 K. Flachbart, S. Gabáni, J. Kačmarčik, T. Mori, S. Otani and V. Pavlík, *AIP Conf. Proc.*, 2006, **850**(1), 635–636.
26 H. Ozisik, E. Deligoz, K. Colakoglu and Y. Ciftci, *Comput. Mater. Sci.*, 2011, **50**, 1057–1063.
27 J. Meléndez-Martınez, A. Domınguez-Rodrıguez, F. Monteverde, C. Melandri and G. De Portu, *J. Eur. Ceram. Soc.*, 2002, **22**, 2543–2549.

28 D. Portehault, S. Devi, P. Beaunier, C. Gervais, C. Giordano, C. Sanchez and M. Antonietti, *Angew. Chem., Int. Ed.*, 2011, **50**, 3262–3265.
29 Q. Yang, J. Lv, Q. Tong, X. Du, Y. Wang, S. Zhang, G. Yang, A. Bergara and Y. Ma, *Phys. Rev. B*, 2021, **103**, 024505.
30 I. Felner, *Phys. C*, 2001, **353**, 11–13.
31 P. Vajeeston, P. Ravindran and H. Fjellvåg, *RSC Adv.*, 2012, **2**, 11687–11694.
32 G. Profeta, A. Continenza, F. Bernardini and S. Massidda, *Phys. Rev. B: Condens. Matter Mater. Phys.*, 2001, **65**, 054502.
33 A. Wallash, J. Crow and Z. Fisk, *J. Magn. Magn. Mater.*, 1986, **54**, 547–548.
34 C. Giannelli, B. Jüttler and H. Speleers, *Computer Aided Geometric Design*, 2012, **29**, 485–498.
35 E. Sanz-Luque, F. Ocana-Calahorro, A. Galván and E. Fernández, *Plant Signaling Behav.*, 2015, **10**, e1042638.
36 C. Pei, J. Zhang, Q. Wang, Y. Zhao, L. Gao, C. Gong, S. Tian, R. Luo, M. Li and W. Yang, *Natl. Sci. Rev.*, 2023, **10**, nwad034.
37 X. Huang, G. Tu, S. Wang, J. Song, Y. Liu and Z. Wang, *Rare Met. Mater. Eng.*, 2022, **51**(3), 1087–1099.
38 A. Drozdov, M. Eremets, I. Troyan, V. Ksenofontov and S. I. Shylin, *Nature*, 2015, **525**, 73–76.
39 D. Duan, Y. Liu, F. Tian, D. Li, X. Huang, Z. Zhao, H. Yu, B. Liu, W. Tian and T. Cui, *Sci. Rep.*, 2014, **4**, 6968.
40 Y. Wang, J. Lv, L. Zhu and Y. Ma, *Physics*, 2010, **82**, 7174–7182.
41 J. Lv, Y. Wang, L. Zhu and Y. Ma, *J. Chem. Phys.*, 2012, **137**, 084104.
42 Y. Wang, L. Jian, Z. Li and Y. Ma, *Comput. Phys. Commun.*, 2012, **183**, 2063–2070.
43 G. G. Kresse and J. J. Furthmüller, *Phys. Rev. B: Condens. Matter Mater. Phys*, 1996, **54**, 11169.
44 A. Gk and B. Jf, *Comput. Mater. Sci.*, 1996, **6**, 15–50.
45 J. P. Perdew and Y. Wang, *Phys. Rev. B*, 2018, **45**, 13244.
46 P. E. Blochl, *Phys. Rev. B: Condens. Matter Mater. Phys*, 1994, **50**, 17953–17979.
47 S. Baroni, S. D. Gironcoli, A. Corso, S. Scuola, I. Superiore, I. Istituto, F. Materia, I. Trieste and P. Giannozzi, *Rev. Mod. Phys.*, 2001, **73**(2), 515.
48 P. Giannozzi, S. Baroni, N. Bonini, M. Calandra, R. Car, C. Cavazzoni, D. Ceresoli, G. L. Chiarotti, M. Cococcioni and I. Dabo, *J. Phys.: Condens. Matter*, 2009, **21**, 395502.
49 J. P. Perdew, K. Burke and M. Ernzerhof, *Phys. Rev. Lett.*, 1996, **77**, 3865.
50 D. Hamann, *Phys. Rev. B: Condens. Matter Mater. Phys.*, 2013, **88**, 085117.
51 P. B. Allen and R. C. Dynes, *Phys. Rev. B: Solid State*, 1975, **12**, 905–922.
52 W. McMillan, *Phys. Rev.*, 1968, **167**, 331.
53 J. Bardeen, L. N. Cooper and J. R. Schrieffer, *Phys. Rev.*, 1957, **108**, 1175.
54 H.-D. Liu, Y.-P. Li, L. Yang, N. Jiao, M.-M. Zheng, H.-Y. Lu and P. Zhang, *Phys. Rev. B*, 2022, **105**, 224501.
55 E. Deligoz, K. Colakoglu, H. Ozisik and Y. Ciftci, *Solid State Sci.*, 2012, **14**, 794–800.
56 S. Aydin and M. Simsek, *Phys. Rev. B: Condens. Matter Mater. Phys.*, 2009, **80**, 134107.